RSC Advances

ROYAL SOCIETY OF CHEMISTRY

www.rsc.org/advances

The Table of Contents entry

Graphic:

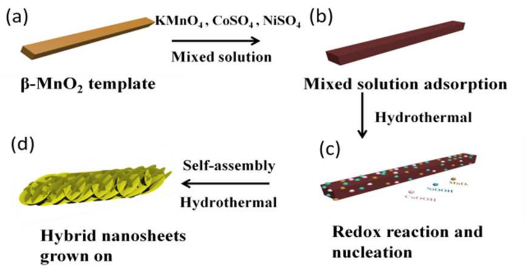

Text:

Nanoflaky (Ni, Co, Mn) oxides have successfully grown on the surface of the β-MnO_2 nanorod via a simple redox reaction.

Preparation and Performance of β-MnO_2 nanorod @ nanoflake (Ni, Co, Mn) oxides with hierarchical mesoporous structure

Hao Wang, Qinglan Zhao, Xianyou Wang*, Youwei Zhang, Jiao Gao,
Yanqing Fu, Xiukang Yang, Hongbo Shu*

(Key Laboratory of Environmentally Friendly Chemistry and Applications of Ministry of Education，Hunan Province Key Laboratory of Electrochemical Energy Storage and Conversion，School of Chemistry, Xiangtan University, Hunan, Xiangtan 411105, China)

Abstract: The rational design and facile synthesis of transition metal oxides are necessary to improve their application in the supercapacitors. Herein three kinds of hierarchical mesoporous structure transition metal oxides, which are composed of a β-MnO_2 nanorod core and one of three different nanosheet hybrid (Ni, Co, Mn) oxide shells, are facilely synthesized via a novel *in situ* nucleation and growth of transition metal oxides on the surface of the β-MnO_2 nanorod. The crystallographic analyses demonstrated that the three kinds of hybrid oxide shells are consisted of cobalt manganese oxide (CMO), nickel manganese oxide (NMO), and nickel cobalt manganese oxide (NCMO), respectively. These transition metal oxides are evaluated as electrodes for high performance supercapacitors (SCs). The results reveal that β-MnO_2@CMO exhibits still a good rate capability of 35% capacity retention even at 20A g^{-1}, while β-MnO_2@NMO displays a high pseudocapacitance of 560 F g^{-1} at 1 A g^{-1}. However, β-MnO_2@NCMO combined the advantages of both β-MnO_2@CMO and β-MnO_2@NMO, exhibits a high specific capacitance of 675 F g^{-1} at 1 A g^{-1} with

---

* **Corresponding author:** Xianyou Wang Tel: +86 731 58292060; fax: +86 731 58292061.
E-mail address: wxianyou@yahoo.com (X. Wang).
* **Corresponding author:** hongboshuxtu@gmail.com

excellent rate performance (about 30% capacity retention at 20A g^{-1}) and cycling stability (83% capacity retention after 3000 cycles). The improved electrochemical performance can be attributed to the unique hierarchical architecture and the synergistic effect of different components.

Key words: Supercapacitor; Composite materials; Transition metal oxides; Core-shell structure, Rate capability

1. Introduction

In recent years, advanced energy storage devices have been extensively researched with the fast growing demand for high-power applications.[1] Especially, supercapacitors (SCs) are considered to be an important renewable energy storage device due to their faster charge/discharge process, longer lifespan, higher reliability and lower maintenance cost.[2, 3] There are three major types of electrode materials reported for SCs, including carbonaceous materials, transition metal oxides or hydroxides, and conducting polymers.[4] Among those electrode materials, the transition metal oxide composite is a kind of promising compound to solve low specific capacitance for carbon-based materials and poor cycling stability for polymers.[5]

Among transition metal oxides, Ni, Co, and Mn oxides, have been extensively studied as promising candidates for SCs because of their variety of oxidation states for charge transfer and high mass density.[6, 7] For example, MnO_2 has a high theoretical specific capacitance of about 1370 F g^{-1}, Co_3O_4 has a theoretical specific capacitance of about 890 F g^{-1}.[8] However, the NiO_2 and Co_3O_4 suffer from poor capacity retention and rate capacity, and the specific capacitance of MnO_2 is still limited due to the low conductivity (10^{-5} to 10^{-6} S cm^{-1}) and low diffusion coefficient of inserted cations.[9, 10] Undoubtedly, it has been reported that the rational design of transition metal oxide composite can provide a promising solution to achieve excellent supercapacitive performance due to the synergistic effects of different components, which can effectively improve the electrochemical performances of the materials.[11] Thus, to address these problems, one strategy is to design MnO_2-based composite oxides with highly conductive transition metal compounds. For example, $NiCo_2O_4@MnO_2$ core-shell nanowire arrays reported by Xu et al. present an improved capacitance (3.31 F cm^{-2} at 2mA cm^{-2}).[12] However, the MnO_2 is generally designed as the shell among most of the MnO_2-based composite transition metal oxides, which is still low conductivity.[13, 14, 15] Even though, many scholars try to prepare MnO_2 as the core of the composites, the shell covered on the surface of the MnO_2 may be not uniform.[16, 17]

In this work, a facile hydrothermal method has been designed to synthesize three hierarchical nanocomposites with a β-MnO_2 nanorod core and hybrid nanosheet shell. As $KMnO_4$ is reduced by low valence metal ions (Ni^{2+}, Co^{2+}) under the hydrothermal process, the resultant MnO_2 and Ni-Co hydroxides are in situ nucleation on the surface of the β-MnO_2 nanorods prepared as the template. The hybrid shell offers several advantages: one is that the β-MnO_2, with stable crystal structure in both nanosheet shells and cores can form a stable framework owing to its high surface areas and interconnected porous nanostructures which could better accommodate structural changes; [18, 19] the other is that the NiO_2, Co_3O_4 or $NiCo_2O_4$ embedded in the framework can improve the conductivity of the composites. Besides, the morphologies and electrochemical properties of the as-prepared three novel composites are discussed in details.

2. Experiment

2.1. Sample synthesis

All the reagents were of analytical grade and used without further purification. The template of β-MnO_2 nanorods was prepared as in Ref.[20] β-MnO_2@CMO nanocomposites are synthesized in a simple process, 0.2 g of as-prepared β-MnO_2 nanorod was dispersed in 75 mL of deionized water and ultrasonic treatment for 30 min, and then 0.2 g $KMnO_4$ and 1.2 g $CoSO_4{\cdot}7H_2O$ were added to form a homogeneous purple solution, followed by stirring for 1h. After that, the above solution was transferred into a Teflon-lined autoclave (100 ml), sealed and put in an electric oven at 120 ^{o}C for 12 h, and then cooled down to ambient temperature naturally. Finally, the precipitation was filtered, washed with distilled water, vacuum dried and then calcined at 350 ^{o}C for 2h in flowing argon at a ramping rate of 1 ^{o}C. The process of synthesis of β-MnO_2@NMO, and β-MnO_2@NCMO nanocomposites are the same as above route. The details are as follows: for β-MnO_2@NMO, 1g $NiSO_4{\cdot}6H_2O$, 0.2 g $KMnO_4$ and 0.2 g β-MnO_2 nanorods were mixed in 75 ml deionized water, then the mixture were maintained at 130 ^{o}C for 24h; while for β-MnO_2@NCMO, the designed amount of $CoSO_4{\cdot}7H_2O$ and $NiSO_4{\cdot}6H_2O$ were mixed with 0.2 g β-MnO_2 nanorods in 75 ml deionized water, and then maintained at 140 ^{o}C

for 12h.

2.2. Physicochemical properties characterization

The crystallographic analyses of samples were carried out by X-ray diffraction (XRD) (D/max-2550 Rigaku, Japan). Morphology of samples was characterized using field-emission scanning electron microscopy (FESEM Nova NanoSEM 230). The morphology and structure of the nanocomposites were further investigated by transmission electron microscopy (TEM) (JEM-2100F, JEOL). The specific surface area and pore structure of the samples were determined by N_2 adsorption/desorption isotherm at 77 K (JW-BK 112) after the prepared samples were degassed at 110 ^{o}C overnight.

2.3. Electrochemical measurements

The working electrodes were prepared by the mixed slurry containing active materials (80 wt%), acetylene black (10 wt%) and polyvinylidene fluoride (PVDF 10 wt%) in N-methyl-2-pyrrolidone (NMP). The slurry was painted onto a nickel mesh with the area of 1 cm^2 then dried and pressed. Electrochemical measurements were performed on an electrochemical workstation (VersaSTAT3, Princeton Applied Research, USA) by using a three-electrode mode in an aqueous KOH (6.0 M) with a nickel mesh and Hg/HgO as the counter and reference electrode.

3. Results and discussion

3.1. Morphology and Structural Analysis

The fabrication processes of the novel architectures are schematically illustrated in Figure 1(a)-(d). The β-MnO_2 nanorod provides a suitable template for homologous

MnO_2 nucleating and growing because the surface of the β-MnO_2 nanorod is consisted of perfect crystals. Firstly, when the β-MnO_2 nanorod was added to the mixed solution containing $KMnO_4$, $CoSO_4$·and $NiSO_4$·or either one of the two low valence sulfates and stirred, the mixed solution will be adsorbed on the surface of the β-MnO_2 nanorod. Then, along with the occurrence of the redox reaction during the hydrothermal process, the reducted product MnO_2 will be *in situ* nucleating on the surface of the β-MnO_2 nanorod, and the metal ions (Ni^{2+}, Co^{2+}) can be oxidized, and then their hydroxides will be nucleated followed by MnO_2. Finally, those novel architectures with hybrid nanosheet shells and a β-MnO_2 nanorod core are easily formed via this simple hydrothermal method. Besides, in the redox reaction process, the quantity of $CoSO_4$ and $NiSO_4$ can be controlled in any desired ratios within certain ranges, and the corresponding products will be obviously different.

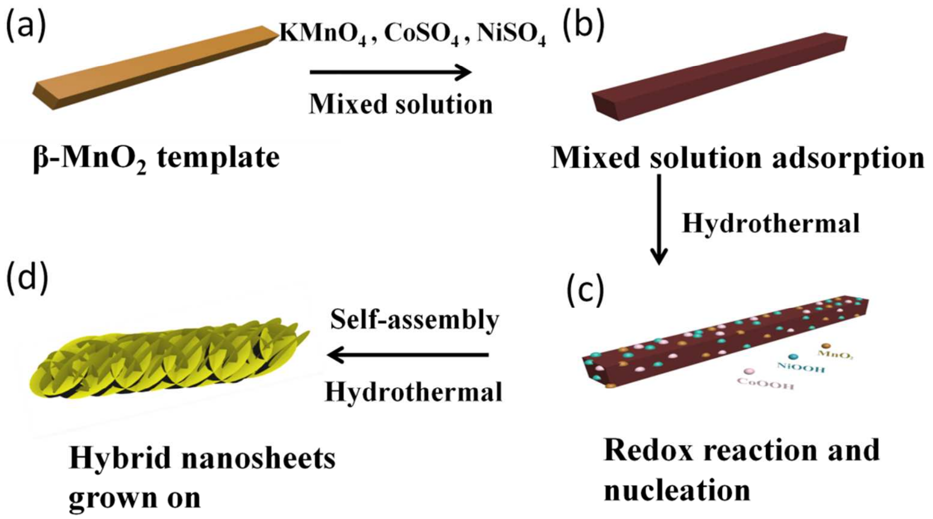

Figure 1 Schematic illustration of the formation of nanoflaky Ni, Co, Mn composite oxides *in situ* growing on the surface of the MnO_2 nanorod.

The morphology of the as-synthesized samples was examined with scanning electron microscopy (SEM). As shown in Figure 2(a-c), Co, Ni and Co-Ni hydroxides grow uniformly on the surface of β-MnO_2 templates in company with MnO_2. The yield of the shell is so high that the β-MnO_2 nanorods with a smooth surface are not observed in the nanocomposites. Obviously, among all composite oxides, the slice of the hybrid shell for β-MnO_2@CMO-precursor is the thickest and tightest. Besides, for β-MnO_2@NMO-precursor and β-MnO_2@NCMO-precursor, the flower texture layer with highly porous structure is uniformly deposited on the surface of the β-MnO_2 nanorods. It also can be seen that the diameter of the β-MnO_2@CMO-precursor is the least, the β-MnO_2@NMO-precursor has the most abundant pores, and β-MnO_2@NCMO-precursor shows the largest pore size and diameter. In addition, these nanoflaky shells are not changed after high temperature annealing as shown in Figure 2(d-f). The stability of those architectures can probably be attributed to the crystal structure of β-MnO_2, which has the most stable structure among all crystals of MnO_2. As a typical example, the low-magnification SEM image of β-MnO_2@CMO is displayed in Figure 2g, it can be seen that the nanocomposites represent uniform distribution. The β-MnO_2 nanorod templates are also displayed in Figure 2h, where the nanorods show a smooth surface and uniform diameter. The porous structures are characterized by BET measurements. As shown in Figure 2i, the nitrogen adsorption/desorption isotherms of all prepared samples are the combination of type II and IV according to the IUPAC classification. The β-MnO_2@NMO possesses the highest BET surface area of 130.9 m^2 g^{-1} with a pore volume of 0.293 cm^3 g^{-1}. The specific surface area and pore volume of β-MnO_2@NCMO are 102 m^2 g^{-1} and 0.216 cm^3 g^{-1}, respectively. Besides, the β-MnO_2@CMO also possesses a high BET surface area are 88.3 m^2 g^{-1} with a pore volume of 0.185 cm^3 g^{-1}. The BJH pore size distributions of β-MnO_2@CMO, β-MnO_2@NMO and β-MnO_2@NCMO are shown in Figure 2i insert. It can be found that the pore sizes of β-MnO_2@CMO, β-MnO_2@NMO and β-MnO_2@NCMO are concentrated at 7.0 nm, 5.5 nm and 6.0 nm, respectively. Obviously, the pore size of β-MnO_2@NCMO is intermediate between those of β-MnO_2@CMO and β-MnO_2@NMO.

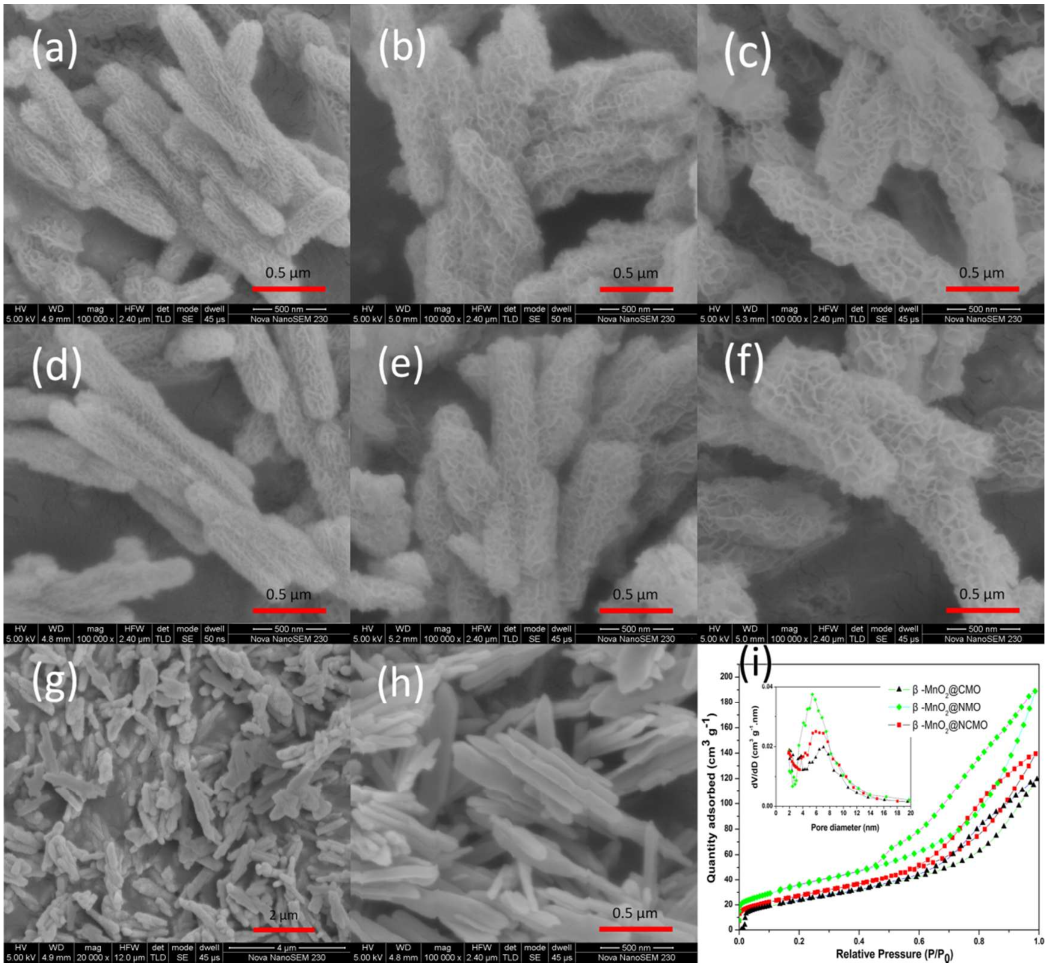

Figure 2 SEM images of (a) β-MnO_2@CMO-precursor; (b)

β-MnO_2@NMO-precursor; (c) β-MnO_2@NCMO-precursor; (d) β-MnO_2@CMO; (e) β-MnO_2@NMO; (f) β-MnO_2@ NCMO; (g) Low-magnification SEM image of β-MnO_2@CMO; (h) β-MnO_2 templates. (i) Nitrogen adsorption-desorption isotherms and pore-size distribution curves (inset) of the nanocomposites nanostructures.

The hierarchical hybrid structure is further illustrated from the TEM images from Figure 3. The low-magnification TEM images show that the surface of β-MnO_2 nanorods is uniformly covered with Ni, Co, Mn composite oxide nanosheets and formed a core-shell structure. In addition, the thickness of the different nanosheets and layers can be contrasted in the TEM images (Figure 3b, e, h). It can be found that the layers of the β-MnO_2@CMO, β-MnO_2@NMO and β-MnO_2@NCMO are about 75 nm, 95 nm and 97 nm thick, respectively. Besides, the slice of the β-MnO_2@NMO is thinner than that of two others. The HR-TEM is used to investigate the lattice of surface layer hybrid metal oxide. The lattice spacing of 0.467 nm and 0.31 nm were observed in Figure 3c, which are in a good agreement with the theoretical interplanar spacing of Co_3O_4 (111) and β-MnO_2 (110) planes. As shown in Figure 3(f, i), the interplanar spacing of 0.31 nm corresponds well to the (110) plane of β-MnO_2, the 0.48 nm and 0.47 nm can correspond to the (003) plane of NiO_2 and (111) plane of $NiCo_2O_4$, respectively. Therefore, it can be concluded that the shells of those nanocomposites are consisted of β-MnO_2 and Ni/Co composite oxides.

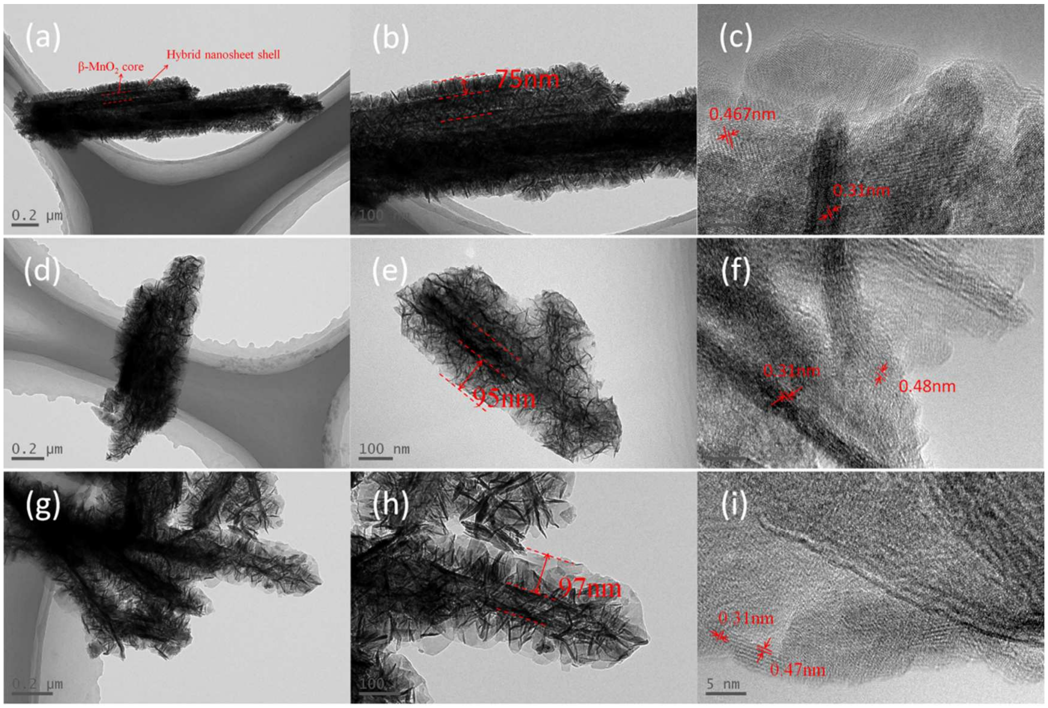

Figure 3 Low-magnification and high-magnification TEM images of (a-c) β-MnO$_2$@CMO; (d-f) β-MnO$_2$@NMO; (g-i) β-MnO$_2$@NiCMO.

The crystallographic structures of the as-prepared β-MnO$_2$ nanorod, β-MnO$_2$@NCMO-precursor and crystalline β-MnO$_2$@NCMO nanocomposite obtained by annealing the precursors at 350 °C for 2h were verified by XRD, as shown in Figure 4a. The diffraction peaks of the MnO$_2$ nanorod represent all of the characteristic peaks of pure pyrolusite-type MnO$_2$ (JCPDS 24-0735) phase without any impurities. And the three broad diffraction peaks are located at around 29°, 37°and 57° in the XRD pattern of MnO$_2$, which correspond to the diffraction bands (110), (101) and (211) of β-MnO$_2$, respectively. Besides, the diffraction peaks of β-MnO$_2$@NCMO-precursor can be well indexed of (Co, Ni)O(OH) (JCPDS 29-0491) apart from the dominant peak of β-MnO$_2$. There is no contaminant detected, indicating that the precursor is composed of β-MnO$_2$ and Ni-Co hydroxide. The patterns of β-MnO_2@NCMO reveal that the nickel cobalt oxide ($NiCo_2O_4$) (JCPDS 20-0781) can be found after the precursor was calcined at 350 °C for 2h. Furthermore, Figure 4b shows that all the diffraction peaks are assigned to pure cobalt oxide (Co_3O_4) (JCPDS 43-1003) and nickel oxide (NiO_2) (JCPDS 85-1977) without any impurity apart from β-MnO_2.

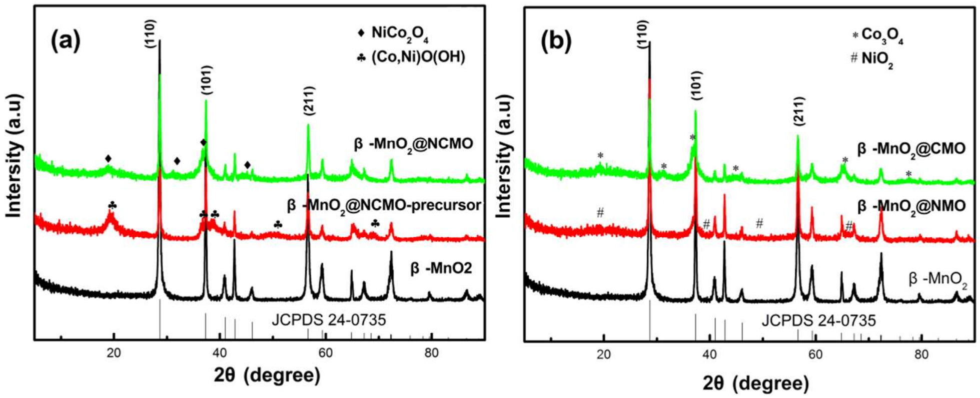

Figure 4 XRD patterns of (a) β-MnO_2, β-MnO_2@NCMO-precursor and crystalline β-MnO_2@NCMO nanocomposites; (b) β-MnO_2, β-MnO_2@CMO and β-MnO_2@NMO nanocomposites.

3.2. Electrochemical Analysis

The supercapacitive performances of as-prepared products were evaluated by electrochemical technology. Figure 5a shows the cyclic voltammograms (CVs) of β-MnO_2 nanorod and nanocomposite electrodes at a scan rate of 5 mV s^{-1}. Clearly, a pair of well-defined redox peaks within 0.1-0.5 V (vs. Hg/HgO) is visible in the CV curve of the pure β-MnO_2, which corresponds to redox couple of MnO_2/MnOOM, where M represents H^+ or K^+ ions.[10] Moreover, it can be seen that the three hybrid nanocomposites have not only the redox peaks of MnO_2 but also a pair of redox peaks within the -0.45-0.1 V (vs. Hg/HgO), which correspond to the reversible reaction of Co^{3+}/Co^{4+} or Ni^{2+}/Ni^{3+} transitions associated with anions OH^-.[21, 22] It is obvious that the integrated area of β-MnO_2@NCMO in the current-potential curve is more than that of any others, and the increase of the CV integrated area will lead to a much more pseudocapacitance.[23] Thus, the β-MnO_2@NCMO gives a highest capacity. This may be ascribed to the synergistic effects of different components. Besides, it can be known from these CV curves that both the hybrid nanosheet shells and the β-MnO_2 core can contribute to the pseudocapacitance of nanocomposite.

Galvanostatic charge-discharge measurements were conducted between -0.45 to 0.5 V (vs. Hg/HgO) at different current densities ranging from 1 to 20 A g^{-1} to further evaluate the properties of the nanocomposites. As shown in Figure 5(b-d), it can be observed that there are two voltage plateaus at around -0.35 and 0.25. The specific capacitance is calculated by the formula, $C = (I\Delta t)/(m\Delta V)$, where I is the discharge current, Δt is the discharge time, ΔV is the voltage range and m is the mass of the active material. The specific capacitance of β-MnO_2@CMO is as high as 437, 395, 250, 200 and 149 F g^{-1}; for β-MnO_2@NMO is about 560, 510, 220, 132 and 70 F g^{-1}, and for β-MnO_2@NCMO is about 675, 593, 357, 254 and 190 F g^{-1} at the current density of 1, 2, 5, 10, 20 A g^{-1}, respectively. The specific capacitances of the three nanocomposite electrodes derived from the discharging curves at different current densities were compared, as shown in Figure 5e. The β-MnO_2@CMO electrode delivered a specific capacitance of 437 F g^{-1} at the current density of 1 A g^{-1}, which is lower than those of β-MnO_2@NMO and β-MnO_2@NCMO electrode. However, at the high current density of 20 A g^{-1}, the β-MnO_2@CMO electrode still delivered a high specific capacitance of 149 F g^{-1}, indicating much better rate capability compared to the β-MnO_2@NMO electrode which has a high specific capacitance of 560 F g^{-1} but decay fast to merely 70 F g^{-1} when the current density increased from 1 A g^{-1} to 20 A g^{-1}. It also can be seen clearly that the β-MnO_2@NCMO electrode exhibits best pseudocapacitance and rate capability among three nanocomposites.

The cycling stability of the nanocomposites and β-MnO_2 nanorod electrodes are evaluated by the repeated charging-discharging measurement at constant current density of 5 A g^{-1}, as shown in Figure 5f. A significant specific capacitance loss can be seen for β-MnO_2 nanorod electrode that only 51% of the initial capacitance is retained after 3000 cycles. While for β-MnO_2@NMO and β-MnO_2@NCMO electrodes, the specific capacitances are about 220 and 360 F g^{-1} in the 1st cycle, and remained 173 and 305 F g^{-1} after 3000 cycles, the corresponding capacitance loss is 21% and 17%, respectively. In addition, the cycling stability of β-MnO_2@CMO is slightly better than that of the other two electrodes, which the capacitance loss is about 14% after 3000 cycles. It can be known that the nanocomposite electrodes show a much better cycling stability than pure β-MnO_2.

The results reveal that β-MnO_2@CMO exhibits a good rate capability, while β-MnO_2@NMO displays a high pseudocapacitance. These differences in performances can be mainly attributed to the morphological characteristics of the mesoporous and the nanosheets architectures, as well as the composition of constituents. Evidently, the mesoporous and nanosheets within those architectures can provide more active sites and path for efficient electrolyte ions transportation.[24] Therefore, the fact that β-MnO_2@NMO displays a much higher pseudocapacitance can be dependent on its much higher BET surface area than β-MnO_2@CMO. Besides, compared with the other two nanocomposites electrodes, β-MnO_2@CMO exhibits the best rate capability. It may be attributed to its largest BJH pore sizes which can facilitate the diffusion of ions and improve chare accumulation. Moreover, β-MnO_2@NCMO combines the advantages of both β-MnO_2@CMO and β-MnO_2@NMO, exhibiting a high specific capacitance and cycling stability. Those good performances can be attributed to not only full utilization of individual constituents, but also a strong synergistic effect of different components. However, since the pure transition metal oxide composites still suffer from low conductivity, some efforts remain to be done to further improve the cycling performance and depress the capacity decay of β-MnO_2@NCMO, such as combination with high conductivity graphene, carbon or conducting polymer.

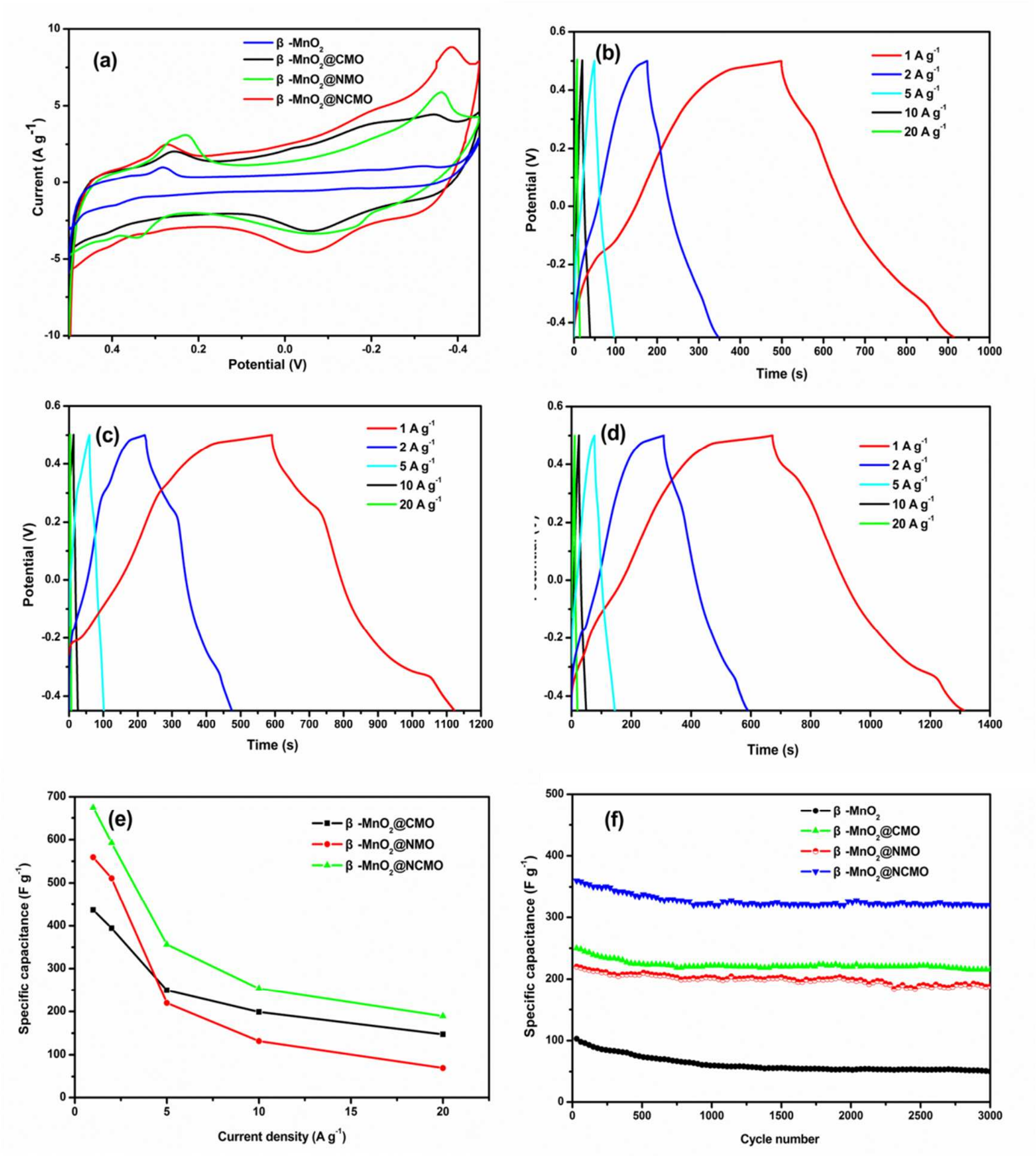

Figure 5 (a) CV curves of as-synthesized samples at a scan rate of 5 mV s^{-1}; Constant-current charge-discharge profiles of (b) β-MnO$_2$@CMO, (c) β-MnO$_2$@NMO, and (d) β-MnO$_2$@NCMO; (e) Specific capacitance of these electrodes at various rates and (f) Cycling stability of as-synthesized samples at a constant current density of 5 A g^{-1}.

Figure 6a shows the CV curves of β-MnO$_2$@NCMO at various scan rates of 5-40 mV s^{-1}. It can be found that with the increase of the scan rate, the shapes of CV curves show slight distortion and the areas surrounded by the CV curves are not significantly influenced, implying good rate capability of the β-MnO_2@NCMO electrode. Electrochemical impedance spectroscopy (EIS) was further employed to detect the properties of ion diffusion and electron transfer in the three kinds of nanocomposite electrodes in the frequency range of 100 kHz to 10 mHz with an AC voltage of 5 mV. The Nyquist plots are shown in Figure 6b and the inset shows the expanded plots at high frequency region. The impedance spectra of three electrodes are almost similar in form with a semicircle at the high frequency and an inclined line following at the low frequency, which corresponds to the interfacial charge-transfer impendence and the diffusive impendence of OH^- ion within the electrode. The slopes of the semicircle at high frequency of the three electrodes are also almost the same, indicating nearly equal value of charge-transfer impendence. The diffusive impendence of OH^- ion within the β-MnO_2@CMO and β-MnO_2@NCMO are much lower than that of β-MnO_2@NMO.

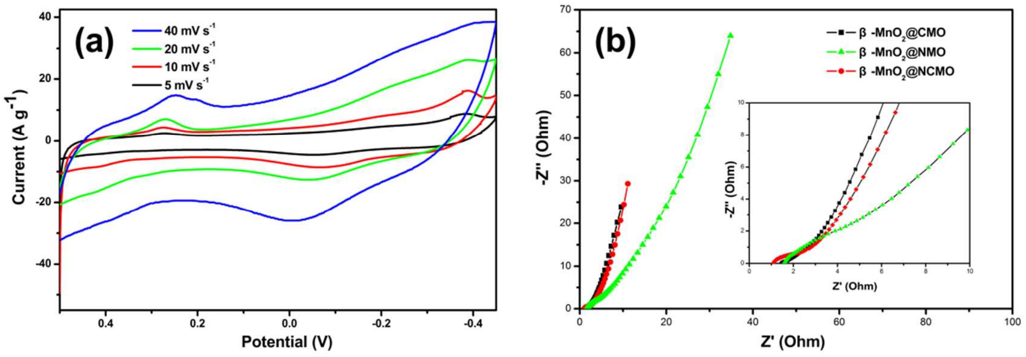

Figure 6 (a) The CV curves of the β-MnO_2@NCMO at different scan rates; (b) Nyquist plots for the three nanocomposite electrodes, the inset is the expanded plots at high frequency region.

4. Conclusion

Accompanying with the formation of MnO_2, the nanoflaky Co_3O_4, NiO_2 and $NiCo_2O_4$ have successfully grown on the surface of the β-MnO_2 nanorod via a simple redox reaction between $KMnO_4$ and Co^{2+}/Ni^{2+} during a hydrothermal process. The electrochemical properties of these three hybrid nanostructured composites are evaluated as electrode materials for SCs and all of them show good electrochemical performance. Especially, the β-MnO_2@NCMO, which has a good rate capability (about 30% capacity retention at 20A g^{-1}) and excellent pseudocapacitance (about 675 F g^{-1} at 1 A g^{-1}), shows superior to both β-MnO_2@CMO and β-MnO_2@NMO which exhibit good rate capability (35% capacity retention at 20A g^{-1}) and high specific capacitance (560 F g^{-1} at 1 A g^{-1}), respectively. In addition, due to the synergistic effect of different metal oxides, the nanocomposites show good cycle stability, which is evidently much better than that of pure β-MnO_2 (only 51% capacity retention after 3000 cycles). Therefore, the hierarchical transition metal oxide composites will be a kind of promising electrode materials for the application of high performance SCs and other energy storage fields, e.g., electrocatalysis and Li-ion batteries.

Acknowledgements

This work is funded by the National Natural Science Foundation of China under project No. 51272221, Scientific and Technical Achievement Transformation Fund of Hunan Province under project No. 2012CK1006, Key Project of Strategic New Industry of Hunan Province under project No. 2013GK4018, and Science and Technology plan Foundation of Hunan Province under project no. 2013FJ4062.

Reference

1. M. Mann, R. Bradley, M. Hughes, *Nature*, 1998, 392, 779.

2. G.Q. Zhang, H.B. Wu, H.E. Hoster, M.B. Chan-Park, X.W. Lou, *Energy Environ. Sci.*, 2012, 5, 9453-9456.

3. P. Yang, Y. Ding, Z. Lin, Z. Chen, Y. Li, P. Qiang, M. Ebrahimi, W. Mai, C.P. Wong, Z.L. Wang. *Nano Lett.*, 2014, 14, 731-736.

4. J. Liu, J. Jiang, C. Cheng, H. Li, J. Zhang, H. Gong, H.J. Fan, *Adv. Mater.*, 2011, 23, 2076-2081.

5. G. Zhang, X.W. Lou, *Sci. Rep.*, 2013, 3, 1470.

6. C. Guan, J. Liu, C. Cheng, H. Li, X. Li, W. Zhou, H. Zhang, H. J. Fan, *Energy Environ. Sci.*, 2011, 4, 4496-4499.

7. X. Wang, X. Han, M. Lim, N. Singh, C.L, Gan, M. Jan, P.S, Lee, *J. Phys. Chem. C*, 2012, 116, 12448–12454.

8. D. Kong, J. Luo, Y. Wang, W. Ren, T. Yu, Y. Luo, Y. Yang C. Cheng, *Adv. Funct. Mater.*, 2014, 24, 3815-3826.

9. Z. Sun, S. Firdoz, E.Y.X. Yap, L. Li, X. Lu, *Nanoscale*, 2013, 5, 4379-4387.

10. O. Ghodbane, J.L. Pascal, F. Favier, *ACS Appl. Mater. Interfaces*, 2009, 1, 1130–1139.

11. J. Jiang, Y. Li, J. Liu, X. Huang, C. Yuan, X.W. Lou, *Adv. Mater.*, 2012, 24, 5166-5180.

12. K. Xu, W. Li, Q. Liu, B. Li, X. Liu, L. An, Z. Chen, R. Zou, J. Hu, *J. Mater. Chem. A*, 2014, 2, 4795-4802.

13. L. Yu, G. Zhang, C. Yuan, X.W. Lou, *Chem. Commum.*, 2013, 49, 137-139.

14. H. Jiang, C. Li, T. Sun, J. Ma, *Chem. Commum.*, 2012, 48, 2606-2608.

15. Q. Li, X.F. Lu, H. Xu, Y.X. Tong, G.R. Li, *ACS Appl. Mater. Interfaces*, 2014, 6, 2726–2733.

16. G. Du, X. Liu, Y. Zong, T.S.A. Hor, A. Yu, Z. Liu, *Nanoscale*, 2013, 5, 4657-4661.

17. D. Yu, J. Yao, L. Qiu, Y. Wang, X. Zhang, Y. Feng, H. Wang, *J. Mater. Chem. A*, 2014, 2, 8465-8471.

18. S. Devaraj, N. Munichandraiah, *J. Phys. Chem. C*, 2008, 112, 4406-4417.

19. J. Chen, F. Cheng, *Acc. Chem. Res.*, 2009, 42, 713-723.

20. F. Cheng, Y. Su, J. Liang, Z. Tao, J. Chen, *Chem. Mater.*, 2009, 22, 898.

21. X. Liu, S. Shi, Q. Xiong, L. Li, Y. Zhang, H. Tang, C. Gu, X. Wang, J. Tu, *ACS Appl. Mater. Interfaces*, 2013, 5, 8790-8795.

22. X. Xia, J. Tu, Y. Zhang, X. Wang, C. Gu, X. Zhao, H.J Fan, *Acs Nano*, 2012, 6, 5531-5538.

23. X. Lu, M. Yu, G. Wang, T. Zhai, S. Xie, Y. Ling, Y. Tong, Y. Li, *Adv. Mater.*, 2013, 25, 267-272.

24. K. Xu, R. Zou, W. Li, Y. Xue, G. Song, Q. Liu, X. Liu, J. Hu, *J. Mater. Chem. A*, 2013, 1, 9107-9113.